Materials Transactions, Vol. 43, No. 4 (2002) pp. 688 to 693

Phase Equilibria in Nb–W-rich Zone of the Nb–W–Si Ternary System

Chaoli Ma[1], Yi Tan[1], Aoki Kasama[1] and Shuji Hanada[2]

[1]*Japan Ultra-high Temperature Materials Research Institute, Ube 755-0001, Japan*
[2]*Institute for Materials Research, Tohoku University, Sendai 980-8577, Japan*

In this paper the solidification behavior and phase stability in Nb–W–Si alloys near the Nb–W binary are described. A partial liquidus surface projection of the Nb–W–Si system is constructed based on the observations of microstructure evolution during solidification. Microstructural and microchemical evidences prove the existence of the following eutectic and peritectic reactions: $L \rightarrow \beta(Nb, W)_5Si_3 + Nb_{ss}$; $L + \beta(Nb, W)_5Si_3 \rightarrow (Nb(W))_3Si$; $L \rightarrow (Nb(W))_3Si + Nb_{ss}$. One invariant point for reaction of $L + \beta(Nb, W)_5Si_3 \rightarrow (Nb(W))_3Si + Nb_{ss}$ is determined near composition Nb–16Si–3W. Moreover, phase stabilities at 1773 K in these alloys are briefly described by identifying the constituent phases after prolonged annealing treatment.

(Received October 16, 2001; Accepted February 19, 2002)

Keywords: *liquidus surface projection, isothermal section, phase equilibria, microstructure, phase diagram, niobium-tungsten-silicon ternary system*

1. Introduction

In-situ composites based on Nb–Si alloys have attracted considerable attentions in the last decade due to their high potential for very high-temperature applications such as advanced turbine engines.[1–4] These composites, generally based on compositions in a Nb-rich region of the Nb–Si phase diagram,[5] consist of high strength-low toughness niobium-silicide Nb_5Si_3 and low strength-high toughness Nb solid solution in equilibrium. This is a typical class of materials to be developed on the basis of the concept of ductile-phase-toughening.[6] To achieve good balance of high-temperature strength and room-temperature fracture toughness in the *in-situ* composites, microstructure control and phase chemistry optimization are the most important issues in developing this kind of material.[4] In dealing with these issues alloying is indispensable. It is known that Mo and/or W additions to Nb alloys remarkably increase their high-temperature strength, but diminish their deformability at room temperature.[7] Our preliminary results[8] demonstrated that both low-temperature deformability and high-temperature strength of Nb/Nb-silicide *in-situ* composite prepared by arc-melting are improved by appropriate amounts of Mo and/or W additions. For better understanding of the alloying behavior, we have investigated the effect of Mo additions on the microstructures of Nb–Si alloys. Based on the obtained results, a partial liquidus projection diagram of Nb–Mo–Si system was constructed.[9] The most important feature of this diagram is the existence of a simple eutectic reaction: $L \rightarrow Nb_{ss} + Nb_5Si_3$, which does not exist in Nb–Si binary system.[5] The cast eutectic exhibits very fine lamella-like morphology and the microstructure is significantly refined by the eutectic reaction. As a result, microcracks induced by thermal stresses in silicide phase are reduced in length and density, which is most likely to be responsible for the improvement of room temperature toughness of these alloys. Similar improvement of mechanical properties has been also observed in W added Nb–Si alloys.[10] Microstructural information is essential to understand the mechanical properties. Therefore, the purpose of the present paper is to investigate the microstructure and phase equilibria in the ternary Nb–W–Si system. On the basis of the obtained results on cast and annealed alloys with Nb–W-rich compositions, the partial liquidus surface projection and an isothermal section diagram at 1773 K are constructed.

2. Background on the Nb–W–Si Ternary Equilibria

In this paper, the Nb–W-rich zone (up to 37.5% Si; all compositions are given in mol percent though the paper, unless otherwise stated) of the Nb–W–Si ternary system is considered. In this area, the Nb–Si binary phase diagram[5] possesses two liquid-solid transformations of (1) eutectic reaction, $L \rightarrow Nb_3Si + Nb_{ss}$ at 2193 K for 18.7%Si; and (2) peritectic reaction, $L + \beta Nb_5Si_3 \rightarrow Nb_3Si$ at 2253 K for 19.5%Si. Similarly, in the binary W–Si phase diagram[5] there is a eutectic reaction, $L \rightarrow W_5Si_3 + W_{ss}$ (W solid solution containing Si) at 2453 K for 32.5%Si. In the binary Nb–W phase diagram,[5] there is a continuous solid solution between Nb and W. On the basis of these three binary phase diagrams, a possible Nb–W–Si liquidus surface projection is proposed in Fig. 1(a). (Fig. 1(b) shows actual compositions and detected boundary lines, which will be described and discussed later). In these diagrams, the Nb solid solution containing W and Si is referred to as Nb_{ss}, Nb_3Si containing W in solid solution as $(Nb(W))_3Si$, and α Nb_5Si_3 containing W in solid solution as α $Nb(W))_5Si_3$. Since β Nb_5Si_3 and W_5Si_3 are isomorphous, β Nb_5Si_3 containing W, or W_5Si_3 containing Nb, in solid solution is referred to as $\beta(Nb, W)_5Si_3$.

As seen in Fig. 1(a), the partial liquidus surface projection is divided into three regions, where Nb_{ss}, $(Nb(W))_3Si$, and $\beta(Nb, W)_5Si_3$ appear as a primary phase from the melt, respectively, by several eutectic grooves and peritectic ridges. The β Nb_5Si_3 forms a continuous solid solution, $\beta(Nb, W)_5Si_3$, with W_5Si_3 from Nb–Si side to W–Si side. Between the two binary eutectics of Nb–Nb_3Si (e_2) and W–W_5Si_3 (e_1), there is a eutectic line e_1e_2, which falls in temperature from 2453 K at e_1 to 2193 K at e_2. The locus of the peritectic ridge from the binary peritectic of $L + \beta Nb_5Si_3 \rightarrow$

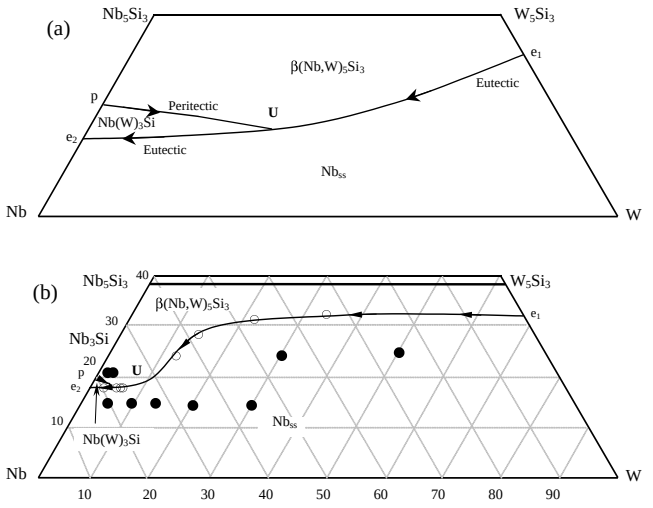

Fig. 1 (a) Schematic showing the proposed partial liquidus surface projection of Nb–W–Si ternary system. Arrows indicate the directions of falling temperatures. (b) Modified liquidus surface projection of Nb–W–Si ternary showing the actual compositions and detected boundary lines.

Nb_3Si intersects the eutectic line and generates a transition reaction:

$$L + \beta(Nb,\ W)_5Si_3 \rightarrow (Nb(W))_3Si + Nb_{ss}.$$

3. Experimental Procedure

The investigated compositions are listed in Table 1. Starting raw materials were elemental powders with the purity of 99.9 mass%Nb, 99.9 mass%W and 99.999 mass%Si. About 20 g buttons were arc melted using a non-consumable electrode on a water-cooled copper crucible under an ultra high-purity argon atmosphere. Alloy buttons were remelted three times to ensure chemical homogeneity. The mass losses were measured for each ingot after melting and were found to be less than 0.1 mass%, suggesting that the alloy compositions were close to their nominal compositions. Samples for heat treatment were cut using an electro-discharge machine (EDM) and annealed at 1973 K for 48 h, followed by furnace cooling to room temperature.

Microstructural observation was preformed using a scanning electron microscope (SEM). The phases and their compositions were determined using X-ray diffraction (XRD) and electron probe microanalysis (EPMA). High-purity Nb, Si and Mo were used as standards and conventional matrix corrections (ZAF) were used to calculate the compositions from the measured X-ray intensities.

4. Results and Discussion

4.1 Liquidus surface

In this section, the microstructural evidence for solidification paths will be described for compositions in each primary phase region, and for compositions near the transition reaction. It should be noted that the actual solidification path might deviate from the equilibrium solidification process, because the melt in our experiments is solidified in a water-cooled copper crucible at a relatively high cooling rate. The phases present in the cast alloys detected by XRD are summarized in Table 1.

Table 1 Alloy compositions and constituent phases of investigated Nb–W–Si alloys.

Region	Composition	Phase in As-Cast Condition
Nb_{ss}-region	Nb–16Si–1W	Primary Nb_{ss} dendrites,
	Nb–16Si–2W	$(Nb(W))_3Si$–Nb_{ss} eutectic
	Nb–16Si–5W	Primary Nb_{ss} dendrites,
	Nb–16Si–10W	$\beta(Nb, W))_5Si_3$–Nb_{ss} eutectic
	Nb–16Si–15W	
	Nb–16Si–20W	
	Nb–16Si–30W	
	Nb–25Si–30W	
	Nb–25Si–50W	
$(Nb(W))_3Si$-region	Nb–19Si–1W	Primary $(Nb(W))_3Si$ dendrites,
	Nb–19Si–2W	$(Nb(W))_3Si$–Nb_{ss} eutectic
$\beta(Nb, W)_5Si_3$-region	Nb–20Si–1W	Primary $\beta(Nb, W)_5Si_3$ dendrites, Peritectic $(Nb(W))_3Si$, $(Nb(W))_3Si$–Nb_{ss} eutectic
	Nb–20Si–3W	Primary $\beta(Nb, W)_5Si_3$ dendrites,
	Nb–25Si–10W	$\beta(Nb, W)_5Si_3$–Nb_{ss} eutectic
Near transition reaction region	Nb–16Si–3W	Primary $\beta(Nb, W)_5Si_3$ dendrites, $\beta(Nb, W)_5Si_3$–Nb_{ss} eutectic, $(Nb(W))_3Si$–Nb_{ss} eutectic

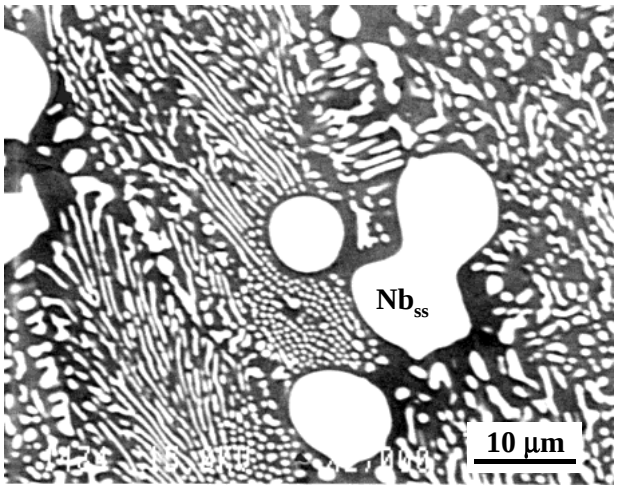

Fig. 2 BEI micrograph of Nb–16Si–1W alloy showing the micromorphologies of eutectic $(Nb(W))_3Si + Nb_{ss}$ and primary phase Nb_{ss}.

4.1.1 Primary Nb_{ss} phase field

The primary Nb_{ss} phase region covers the Nb_{ss}-rich side of $(Nb(W))_3Si + Nb_{ss}$ eutectic and $\beta(Nb,\ W)_5Si_3 + Nb_{ss}$ eutectic valleys, as shown in Fig. 1. Figure 2 shows a typical backscattered SEM micrograph of Nb–16Si–1W alloy in the as cast condition. The microstructure consists of large, bright, nonfaceted primary dendritic particles together with a two-phase mixture formed by a eutectic reaction. The large dendritic particles were identified using EPMA and XRD to be Nb_{ss} with an average composition of Nb–3.3Si–1.6W. The eutectic contains very fine light needles or rods in a gray contrast matrix. EPMA result showed that the gray contrast phase had a composition of Nb–25.1Si–0.4W. The Si concentration is essentially the stoichiometric composition of a Nb_3Si-type phase. XRD data confirmed the presence of a Nb_3Si-type

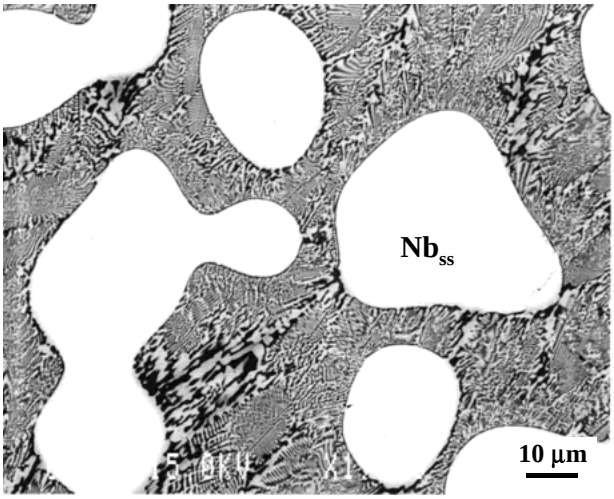

Fig. 3 BEI micrographs of Nb–16Si–5W alloy showing the lamella-like morphology of eutectic $\beta(\mathrm{Nb,\ W})_5\mathrm{Si}_3 + \mathrm{Nb}_{ss}$.

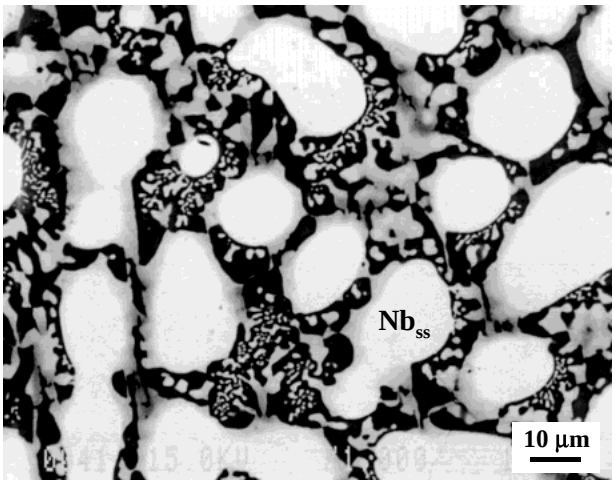

Fig. 4 BEI micrograph of Nb–16Si–20W alloy showing the irregular eutectic structure of $\beta(\mathrm{Nb,\ W})_5\mathrm{Si}_3 + \mathrm{Nb}_{ss}$.

phase, and its x-ray diffraction peaks were much consistent with those of the Nb_3Si (JCPDS card 22-0763). Thus, the gray continuous phase is reasonably identified to be Nb_3Si containing W in solid solution, *i.e.*, $(Nb(W))_3Si$. The light needles or rods in the eutectic are the Nb_{ss}. Therefore, the eutectic reaction can be described as $L \rightarrow Nb_{ss} + (Nb(W))_3Si$. This suggests the composition Nb–16Si–1W is hypoeutectic and close to the $L \rightarrow (Nb(W))_3Si + Nb_{ss}$ eutectic groove. The solidification reaction sequences in this alloy can be described as follows:

$$L \rightarrow Nb_{ss} + L, \quad \text{then}$$

$$L \rightarrow Nb_{ss} + (Nb(W))_3Si.$$

The eutectic $Nb_{ss} + (Nb(W))_3Si$ phase has a similar morphology to that of the eutectic $Nb_{ss} + Nb_3Si$ phase observed in cast Nb–16Si alloy,[10–12] suggesting a weak effect of the small W additions on the eutectic morphology. The eutectic composition was determined by EPMA to be Nb–20.1Si–0.9W. For accuracy, at least five measurements were carried out on selected $10\,\mu m \times 10\,\mu m$ areas that contain the eutectic structure.

Figure 3 illustrates the back-scattered SEM micrograph of Nb–16Si–5W in the as cast condition. This microstructure contains primary Nb_{ss} dendrites and an interdendritic eutectic. The primary Nb_{ss} phase can be easily identified by its large nonfaceted particle morphology and its bright contrast in BEI micrograph. The interdendritic eutectic shows very fine lamellar-like morphology that distinctly differs from that of $Nb_{ss} + Nb_3Si$ type eutectic shown in Fig. 2. EPMA and XRD results revealed that the bright contrast phase in the eutectic is Nb_{ss} and the dark is β Nb_5Si_3-type silicide, *i.e.* $\beta(\mathrm{Nb, W})_5\mathrm{Si}_3$, suggesting a eutectic reaction of $L \rightarrow Nb_{ss} + \beta(\mathrm{Nb,\ W})_5\mathrm{Si}_3$. Therefore, the solidification process in this alloy can be described by:

$$L \rightarrow Nb_{ss} + L, \quad \text{then}$$

$$L \rightarrow Nb_{ss} + \beta(\mathrm{Nb,\ W})_5\mathrm{Si}_3.$$

It is noteworthy that the morphologic features of this eutectic $Nb_{ss} + \beta(\mathrm{Nb,\ W})_5\mathrm{Si}_3$ are similar to those of the eutectic $Nb_{ss} + \beta(\mathrm{Nb,\ Mo})_5\mathrm{Si}_3$ observed in the Nb–Mo–Si ternary system.[9] From the result that no reaction corresponding to $L \rightarrow Nb_{ss} + \beta(\mathrm{Nb,\ W})_5\mathrm{Si}_3$ exists in Nb–Si[5] or Nb–Ti–Si[13] system, it is suggested that a sufficient amount of W and/or Mo addition changes the phase separation behavior during solidification. Moreover, the most important fact that attracts great interest is that one could control the multiphase (Nb/Nb–Silicide) microstructures more easily by utilizing the simple eutectic separation nature in a melting process.

As indicated in Table 1, the simple eutectic reaction exists in the very wide range of W concentration. Several other compositions are also investigated in this region to examine the compositional effect on the eutectic microstructures. With increasing W concentration, the microstructure becomes irregular in the cast eutectic, and W segregation tends to increase at the core of Nb_{ss} particles. As an example, the cast microstructure of Nb–16Si–20W is shown in Fig. 4. No lamella-like eutectic microstructures are seen in this BEI micrograph. Instead, irregular shaped Nb_{ss} particles are distributed in the eutectic. It is also noted that some primary Nb_{ss} particles are surrounded by thin Nb_{ss} "shell", which is identified by light-gray contrast. Composition analysis revealed the outer "shell" is of an average composition of Nb–0.5Si–18.2W, which is the same composition as eutectic Nb_{ss}, but W-poor comparing with that of inner part of the primary Nb_{ss} particles. W concentration in the core of primary Nb_{ss} particles is about 34%. It is likely that the outer "shell" is produced by the nucleation and growth of the eutectic Nb_{ss} on the primary Nb_{ss} particles. Such "shell" structures are often observed in alloys containing moderate W concentrations of 15 to 25%.

To determine the location of the eutectic trough in the ternary space, the average compositions of eutectic in studied alloys are measured by EPMA. At least five measurements were carried out on selected scanning areas that are some $10\,\mu m \times 10\,\mu m$ squares and contain the finest eutectic structure. The results are summarized in Table 2 and plotted in Fig. 1(b). From this figure, it can be seen that the eutectic trough shifts quickly to Si-rich compositions in the range of W contents from 10% to 20%. The reason is unclear, but the non-equilibrium solidification process may be concerned.

Table 2 Average compositions of eutectic Nb_{ss}-$\beta(Nb,W)_5Si_3$ in same studied alloys.

Alloy	Eutectic composition
Nb–16Si–3W	Nb–20.1Si–2.1W
Nb–20Si–3W	Nb–21.6Si–3.1W
Nb–16Si–5W	Nb–20.5Si–2.8W
Nb–16Si–10W	Nb–20.9Si–4.5W
Nb–16Si–15W	Nb–25Si–10.2W
Nb–25Si–30W	Nb–31.9Si–21.3W
Nb–25Si–50W	Nb–33.5Si–30.2W

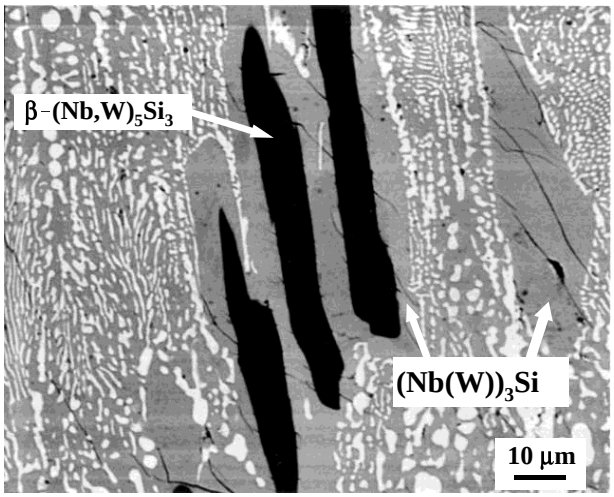

Fig. 5 BEI micrograph of Nb–20Si–1W alloy showing the typical microstructures of peritectic reaction: $L + \beta(Nb, W)_5Si_3 \rightarrow (Nb(W))_3Si$.

4.1.2 Primary $\beta(Nb, Mo)_5Si_3$ phase field

The primary $\beta(Nb,W)_5Si_3$ phase field covers the $\beta(Nb,W)_5Si_3$-rich side of $L+\beta(Nb, W)_5Si_3 \rightarrow (Nb(W))_3Si$ peritectic, and β-$(Nb,Mo)_5Si_3$–Nb_{ss} eutectic valleys. Figure 5 illustrates a BEI micrograph of Nb–20Si–1W alloy, in which some dark distinct particles are located at center areas of large gray dendrites. This is typical peritectic-type morphology. The dark particles were identified to be $\beta(Nb,W)_5Si_3$ using EPMA and XRD, whilst the large gray dendrites to be $(Nb(W))_3Si$. This suggests a peritectic reaction of $L + \beta(Nb, W)_5Si_3 \rightarrow (Nb(W))_3Si$. In the interdendritic area is the eutectic of $(Nb(W))_3Si + Nb_{ss}$. The eutectic consists typically of fine-scale Nb_{ss} rods in $(Nb(W))_3Si$ matrix, which is analogous to that observed in Nb–16Si–1W, as shown in Fig. 2. A few single $(Nb(W))_3Si$ phase particles are occasionally observed in the eutectic matrix. Additionally, numerous microcracks are visible in $(Nb(W))_3Si$ particles, which form during cooling.

This microstructure suggests that the composition of Nb–20Si–1W is hyperperitectic and close to the $L + \beta(Nb, W)_5Si_3 \rightarrow (Nb(W))_3Si$ peritectic ridge. Upon cooling, the $\beta(Nb,W)_5Si_3$ phase nucleates and grows within the melt. The melt composition shifts to meet the peritectic ridge. This leads to solidification of peritectic $(Nb(W))_3Si$ at the surface of primary β-$(Nb,W)_5Si_3$ dendrites. However, the liquid composition only follows the peritectic ridge for a short distance, and it drops off this ridge into the lower primary $(Nb(W))_3Si$ phase region. This leads to solidification of $(Nb(W))_3Si$ phase. The liquid composition continues to move down to the $(Nb(W))_3Si$-rich region and meets the eutectic $Nb_{ss} + (Nb(W))_3Si$ groove. This leads to solidification of the eutectic $Nb_{ss} + (Nb(W))_3Si$.

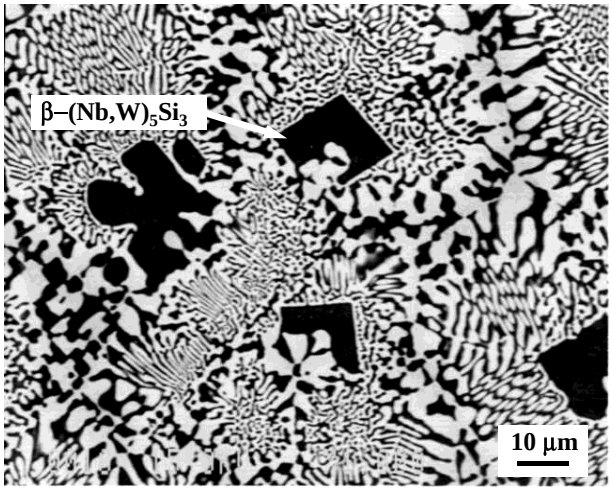

Fig. 6 BEI micrographs of Nb–20Si–3W alloy showing the morphologic features of $\beta(Nb, W)_5Si_3$ primary phase.

Figure 6 illustrates a typical BEI micrograph of hypereutectic Nb–20Si–3W alloy giving rise to primary $\beta(Nb, W)_5Si_3$ dendrites and $Nb_{ss} + \beta(Nb, Mo)_5Si_3$ eutectic. The primary $\beta(Nb,W)_5Si_3$ phase, which is characterized by dark contrast in the BEI micrograph, shows predominantly faceted dendritic morphology. The mean compositions of the primary $\beta(Nb, W)_5Si_3$ and Nb_{ss} in the eutectic are Nb–38.4Si–0.7W and Nb–2.7Si–3.5W, respectively, and the eutectic has a mean composition of Nb–21.5Si–2.9W. No eutectic $Nb_{ss} + (Nb(W))_3Si$ was observed, suggesting that the liquid never reaches the transition point (trip point, namely U in Fig. 1), and the W concentration at the transition is very low.

4.1.3 $(Nb(W))_3Si$-region

In the binary Nb–Si phase diagram,[5] the primary Nb_3Si phase exists in a narrow Si content range from 18.7 to 19.5%. This situation is similar in the ternary Nb–W–Si diagram. The primary $(Nb(W))_3Si$ phase region lies between the $L + \beta(Nb, W)_5Si_3 \rightarrow (Nb(W))_3Si$ peritectic ridge and the $Nb_{ss} + (Nb(W))_3Si$ eutectic groove. As described above, the Nb–16Si–1W is hypoeutectic (see Fig. 2), while the composition of Nb–20Si–1W is hyperperitectic (see Fig. 5). This gives evidence for the narrow $(Nb(W))_3Si$-region between the $(Nb(W))_3Si + Nb_{ss}$ eutectic groove and $L+\beta(Nb, W)_5Si_3 \rightarrow (Nb(W))_3Si$ peritectic ridge.

Figure 7 is the typical microstructure of Nb–19Si–1W. This microstructure consists of primary $(Nb(W))_3Si$ phase and two-phase eutectic $(Nb(W))_3Si$–Nb_{ss} matrix. The primary $(Nb(W))_3Si$ shows large faceted particle morphology. It is noted that the morphology of primary $(Nb(W))_3Si$ phase is similar to that of the primary Nb_3Si phase observed in cast binary Nb–Si alloys.[12] The mean composition of $(Nb(W))_3Si$ dendrites is Nb–26.3Si–0.6W. The Si concentration is slightly higher than the stoichiometric composition. A crack going through the $(Nb(W))_3Si$ faceted particle is seen, suggesting the brittleness of the monolithic $(Nb(W))_3Si$ phase.

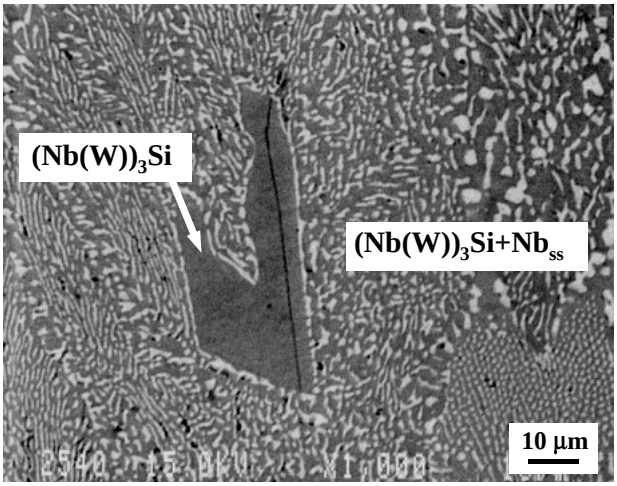

Fig. 7 BEI micrographs of Nb–19Si–1W showing morphologic features of $(Nb(W))_3Si$ primary phase.

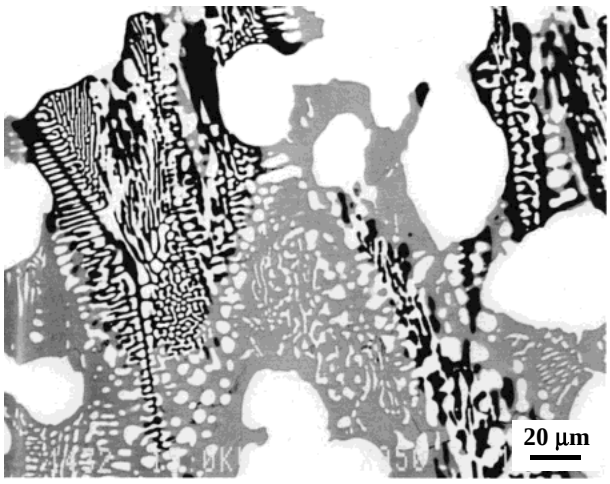

Fig. 8 BEI micrographs of Nb–16Si–3W alloy showing the mixing area of two different eutectics of $\beta(Nb, W)_5Si_3 + Nb_{ss}$ and $(Nb(W))_3Si + Nb_{ss}$.

4.1.4 Composition near transition reaction

As suggested in Fig. 1, the locus of the peritectic ridge from the binary peritectic of $L + \beta Nb_5Si_3 \rightarrow Nb_3Si$ intersects the eutectic groove and generates a transition reaction: $L + \beta(Nb, W)_5Si_3 \rightarrow (Nb(W))_3Si + Nb_{ss}$. As described above, the microstructure of Nb–16Si–2W alloy contains only one kind of eutectic $(Nb(W))_3Si + Nb_{ss}$ (see Fig. 2), while Nb–16Si–5W contains completely different eutectic of $Nb_{ss} + \beta(Nb, W)_5Si_3$ (see Fig. 3). Thus the transition point is expected to be between the two compositions. Nb–16Si–3W was investigated to identify the transition reaction point and microstructure. Microstructural observation in the cast ingot revealed that, there is a large region of eutectic $\beta(Nb, Mo)_5Si_3 + Nb_{ss}$ at a bottom zone of the ingot, and a larger region of eutectic $(Nb(W))_3Si + Nb_{ss}$ at an upper zone, while a middle region is composed of a mixture of these two eutectics. Some primary Nb_{ss} particles are distributed in eutectics matrix. Figure 8 illustrates a BEI micrograph of this region. The eutectic of $(Nb(W))_3Si + Nb_{ss}$ was identified by the gray contrast of $(Nb(W))_3Si$ in BEI image, and the eutectic of $\beta(Nb, W)_5Si_3 + Nb_{ss}$ was identified by the dark contrast of $\beta(Nb, W)_5Si_3$.

The microstructure analysis suggests that the Nb–16Si–3W composition lies on the Nb_{ss}-rich side of eutectic $\beta(Nb, W)_5Si_3 + Nb_{ss}$ valley and near the transition reaction point. On the basis of the proposed diagram, a possible equilibrium solidification route can be described as follows:

1. $L \rightarrow Nb_{ss} + L$; followed by
2. $L \rightarrow \beta(Nb, W)_5Si_3 + Nb_{ss} + L$; followed by
3. $L + \beta(Nb, W)_5Si_3 \rightarrow (Nb(W))_3Si + Nb_{ss} + L$; then
4. $L \rightarrow (Nb(W))_3Si + Nb_{ss}$

It is not difficult to find microstructural evidences for reactions 1 and 2. But the products of reactions 3 and 4 are the same, the eutectic $(Nb(W))_3Si + Nb_{ss}$. It is noted that the transition reaction 3 is peritectic-type and would occur on the $\beta(Nb, W)_5Si_3$ surface when the liquid composition reaches the transition reaction point. Since the arc melted ingots are rapidly cooled after solidification on the water-cooled copper crucible, atom diffusion in a solid phase will be suppressed or retarded. Thus, reaction 3 might not be completed. It is therefore likely that the large volume fraction of eutectic $(Nb(W))_3Si + Nb_{ss}$ phase is produced by the eutectic reaction 4, $L \rightarrow (Nb(W))_3Si + Nb_{ss}$, rather than the transition reaction.

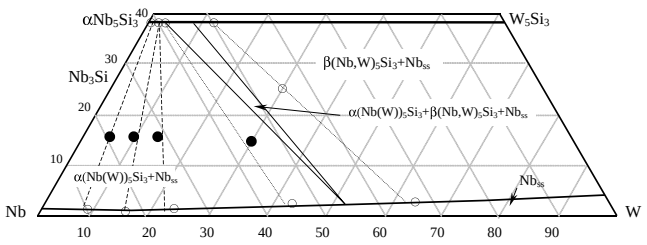

Fig. 9 An isothermal section diagram of Nb–W–Si ternary system at 1973 K. The nominal compositions of tested alloys are shown as solid circles and the phase compositions measured by EPMA are shown as open circles.

4.2 Isothermal section at 1973 K

The phase equilibria at 1973 K were investigated for the ternary Nb–W–Si alloys homogenized at 1973 K for 48 h. In this section, we will give a brief description of these obtained results, which are summarized in Fig. 9. In this diagram, the solid circles indicate the nominal alloy compositions, the open circles do the phase compositions, and the dashed lines do tie lines. The partial phase diagram contains two two-phase regions, $\alpha(Nb(W))_5Si_3 + Nb_{ss}$, and $\beta(Nb, W)_5Si_3 + Nb_{ss}$, and one three-phase region, $\alpha(Nb(W))_5Si_3 + \beta(Nb, W)_5Si_3 + Nb_{ss}$. Though no composition in the $\alpha(Nb(W))_5Si_3 + \beta(Nb, W)_5Si_3 + Nb_{ss}$ three-phase region was investigated in this work, XRD and EPMA results revealed that the silicide phase in Nb–16Si–30W alloy is $\alpha(Nb(W))_5Si_3$ with a composition of Nb–38.5Si–1.5W, while the silicide in Nb–25Si–30W alloy is $\beta(Nb, W)_5Si_3$. Thus, a three-phase region of $\beta(Nb, W)_5Si_3 + \alpha(Nb(W))_5Si_3 + Nb_{ss}$ must exist between the two tie lines through the compositions of Nb–16Si–30W and Nb–25Si–30Mo, respectively. The $\alpha(Nb(W))_5Si_3$ single phase region is very narrow and the maximum solubility of W in $\alpha(Nb(W))_5Si_3$ phase is estimated to be $\sim 2\%$.

5. Conclusions

Three phases of $\beta(Nb, W)_5Si_3$, $(Nb(W))_3Si$, and Nb_{ss} exist in the Nb–W-rich zone of as-cast ternary Nb–W–Si alloys. The phases observed were dendritic, peritectic, or eutectic in nature, depending on the composition and solidification path. The partial liquidus surface projection possesses a transition reaction of $L + \beta(Nb, W)_5Si_3 \rightarrow (Nb(W))_3Si + Nb_{ss}$. The transition reaction occurs at a composition near Nb–16Si–3W. The eutectic and peritectic reactions included in this partial diagram are summarized as follows:

$$L \rightarrow \beta(Nb,\ W)_5Si_3 + Nb_{ss}$$

$$L + \beta(Nb,\ W)_5Si_3 \rightarrow (Nb(W))_3Si$$

$$L \rightarrow (Nb(W))_3Si + Nb_{ss}$$

A partial isothermal section of Nb–W–Si ternary system at 1973 K has been proposed. This phase diagram contains two equilibrium two-phase fields of $\alpha(Nb(W))_5Si_3 + Nb_{ss}$ and $\beta(Nb,\ W)_5Si_3 + Nb_{ss}$, and a three-phase field of $\alpha(Nb(W))_5Si_3 + \beta(Nb,\ W)_5Si_3 + Nb_{ss}$. The solubility of W in $\alpha(Nb(W))_5Si_3$ phase is estimated to be about 2%.

Acknowledgements

This study was performed in Japan Ultra-high Temperature Materials Research Institute and supported by a grant from the New Energy and Industrial Technology Development Organization (NEDO) of Japan.

REFERENCES

1) B. P. Bewlay, J. J. Lewandowski and M. R. Jackson: JOM **49** (8) (1997) 44–45.
2) M. R. Jackson, B. P. Bewlay, R. G. Rowe, D. W. Skelly and H. A. Lipsitt: JOM **48** (1) (1996) 39–44.
3) P. R. Subramanian, M. G. Mendiratta and D. M. Dimiduk: JOM **48** (1) (1996) 33–38.
4) S. Hanada: *Reports of the 123 committee on Heat-Resisting Metals and Alloys*, (JSPS, 38, 1997) pp. 299–307.
5) T. B. Massalski, H. Okamoto, P. R. Subramanian and L. Kacprzak: *Binary Alloy Phase Diagrams*, (ASM, Metals Park, Ohio, 1992) pp. 2767–3378.
6) D. L. Davidson: JOM **49** (8) (1997) 34–34.
7) R. T. Begley: *Evolution of Refractory Metals and Alloys*, edi. by E. N. C. Dalder, T. Grobstein and C. S. Olsen (The Minerals, Metals & Materials Society, TMS, Warrendale, 1994) pp. 29–48.
8) C. L. Ma, H. Tanaka, Y. Tan, A. Kasama, R. Tanaka, Y. Mishima and S. Hanada: Collected of the 1999 Fall Meeting Abstracts of the Japan Inst. Metals (1999) pp. 310–310.
9) C. L. Ma, Y. Tan, H. Tanaka, A. Kasama, R. Tanaka, Y. Mishima and S. Hanada: Mater. Trans., JIM **41** (2000) 1329–1336.
10) C. L. Ma, A. Kasama, Y. Tan, H. Tanaka, R. Tanaka, Y. Mishima, and S. Hanada: *Report of the 123rd Committee on Heat-Resisting Materials and alloys*, (JSPS, 40, 1999) pp. 335–348.
11) C. L. Ma, A. Kasama, H. Tanaka, Y. Tan, R. Tanaka, Y. Mishima and S. Hanada: Mater. Trans., JIM **41** (2000) 719–726.
12) M. G. Mendiratta, J. J. Lewandowski and D. M. Dimiduk: Metall. Trans. A **22A** (1991) 1573–1583.
13) B. P. Bewlay, M. R. Jackson and H. A. Lipsitt: Journal of Phase Equilibria **18** (3) (1997) 264–278.